Feedback regulation by the RhoA-specific GEF ARHGEF17 regulates actomyosin network disassembly

Vasundhara Rao [1,2], Benjamin Grädel [1,2,*], Lucien Hinderling [1,2*], Jakobus Van Unen [1,3], Olivier Pertz [1]

[1] Institute of Cell Biology, University of Bern, 3012 Bern, Switzerland

[2] Graduate School for Cellular and Biomedical Sciences, University of Bern, Bern, Switzerland

[3] Current address: Projekt Epic, Schwarztorstrasse 96, 3007 Bern, Switzerland

[*] Both authors contributed equally

Abstract

We report that the RhoA-specific guanine nucleotide exchange factor ARHGEF17 localizes at the back of a fibroblast's contractile lamella and regulates its disassembly. This localization emerges through retrograde ARHGEF17 transport together with actomyosin flow that most likely involves interactions with ATP-actin at F-actin barbed ends. During this process, ARHGEF17 increasingly oligomerizes into clusters that co-localize with myosin filaments, and correlate with their disassembly at lamella's distal edge. ARHGEF17 loss of function leads to decreased RhoA activity at the lamella back and impairs its disassembly. High RhoA activity is however maintained at the lamella front where phosphorylated myosin light chain is observed. We propose that the low contractile, disassembling actomyosin network at the lamella back generates barbed ends leading to ATP-actin production, and ARHGEF17 binding. This then locally activates RhoA-dependent contractility, ensuring robust lamella disassembly through fracturing rather than re-inforcement. ARHGEF17 exemplifies the spatio-

temporal complexity of Rho GTPase signaling and the requirement of feedback mechanism for homeostasis of contractile actomyosin networks.

Introduction

Rho GTPases regulate cytoskeletal dynamics essential for cell/tissue morphogenesis (Etienne-Manneville and Hall, 2002). Their (in)activation are orchestrated by Guanine nucleotide exchange factors (GEFs) and GTPase Activating Proteins (GAPs). In their GTP-bound state, Rho GTPases activate downstream effectors to modulate cytoskeletal dynamics. Initial studies, based on population-averaged activity measurements and dominant mutants involved Rac1 in lamellipodial extension, Cdc42 in filopodial protrusion, and RhoA in myosin-driven contractility.

Fluorescence Resonance Energy Transfer (FRET)-based biosensors unveiled more complex regulation (Itoh et al., 2002; Kraynov et al., 2000; Nalbant et al., 2004; Pertz et al., 2006) in which RhoA/Rac1/Cdc42 exhibit specific spatio-temporal signaling patterns that fluctuate on time scales of tens of seconds during leading edge protrusion/retraction cycles (Machacek et al., 2009). Adding to this complexity, distinct RhoA/Rac1/Cdc42 signaling patterns are observed at the leading edge upon application of promigratory cues (Martin et al., 2016). The finding of such complex spatio-temporal Rho GTPase signaling patterns must involve precise regulation by GEFs/GAPs. Signaling pattern formation involves Rho GTPase flux, that consists of sequential spatially regulated events such as GEF-triggered Rho GTPase GTP-loading, its diffusion within the plasma membrane, and GAP-mediated inactivation. Ubiquitous GEF/GAP expression, observed across cellular systems (Rossman et al., 2005), is consistent with this complexity.

Comprehensive screening of their subcellular localization revealed that many GEFs/GAPs bind to cytoskeletal and adhesion structures (Müller et al., 2020), suggesting the existence of feedback regulation. By example, Rac1-specific GEFs versus GAPs respectively localize to adhesion structures at the front versus the back of the leading edge (Mueller et al., 2020). Thus, mechanical cues at adhesions at specific subcellular locations control the leading edge Rac activity gradient by spatially recruiting different GEFs/GAPs. Similarly, mechanosensitive interactions between the RhoGAP DLC1 and Talin allows its dissociation from focal adhesions under tension, locally increasing RhoA activity leading to positive feedback for robust and irreversible adhesion disassembly (Heydasch et al., 2023). Further, RhoGAP binding to F-actin provides spatial feedback shaping RhoA activity waves (Bement et al., 2024). Thus, interactions between GEFs/GAPs and cytoskeletal/adhesion structures provides feedback modalities that shape Rho GTPase signaling patterns. Traditional genetic manipulation techniques, which induce long-term changes in cellular states, do not adequately capture such spatio-temporal feedbacks. New methodologies are required to dynamically probe the Rho GTPase flux at adequate length and time scales in single cells.

Consistently with this signaling complexity, leading edge dynamics cycles involve two distinct yet interconnected structures, the lamellipodium and the lamella (Ponti et al., 2004; Small et al., 2002). The lamellipodium explores the environment, forming new protrusions and guiding the direction of movement. The lamella follows, consolidates protrusions into stable adhesions, and generates the contractile forces to pull the cell forward. This strongly suggests that multiple signaling modules must exist to spatio-temporally regulate these different cytoskeletal polymers.

77 Beyond Rho GTPase regulation, the self-organisation properties of the actomyosin
78 cortex feed into regulation of morphogenetic processes. The actomyosin cortex can
79 be understood as an active contractile matter that spontaneously form patterns such
80 as waves, rings, or aggregates due to instabilities in the distribution of contractile
81 forces (Salbreux et al., 2012). Experiments with isolated actomyosin systems have
82 shown that the contractile activity of myosin motors can amplify small fluctuations in
83 the distribution and alignment of actin filaments in a self-reinforcement manner that
84 can result in structural changes such as buckling, fracturing or aggregate formation,
85 that lead to tension loss (Ideses et al., 2018). Cells must therefore deal with
86 emergence of potential catastrophic contractile instabilities in cells.
87
88 An interesting GEF that mediates crosstalk from the cytoskeleton to Rho GTPase
89 signaling is the RhoA-specific GEF ARHGEF17, also known as Tumor Endothelial
90 Marker 4 (Mitin et al., 2013, 2012). ARHGEF17 is characterized by an N-terminal actin-
91 binding domain that exhibits a 90-fold higher affinity for ATP versus ADP-actin, and
92 thus must bind to newly assembled F-actin filaments (Mitin et al., 2012; Prifti et al.,
93 2022) (Fig. 1A). This is followed by a catalytic DH-PH domain, and a C-terminal WD40
94 propeller domain that might regulate protein-protein interactions. *In vitro* studies have
95 shown that ARHGEF17 is specific for Rho isoforms (RhoA, RhoB, RhoC) over Rac1
96 and Cdc42 (Bagci et al., 2020; De Toledo et al., 2000; Mitin et al., 2012; Rümenapp
97 et al., 2002a). This was later also found in a FRET biosensor assay that was used for
98 mapping the specificities of all GEFs/GAPs for specific Rho GTPases in living cells
99 (Müller et al., 2020). Expression of ARHGEF17 DH-PH domains leads to robust
100 contractility (Mitin et al., 2012), further suggesting that it acts as a regulator of RhoA.
101 ARHGEF17 therefore is highly likely to mediate cytoskeletal - Rho GTPase feedback,

102 but the function of this feedback in the spatio-temporal regulation of signaling remains
103 unclear.
104
105 Here, we show that ARHGEF17 dynamically localizes to the lamella back in spreading
106 REF52 fibroblasts. ARHGEF17 oligomerizes from small to larger clusters as it travels
107 with actomyosin retrograde flow. In the edge proximal lamella region, ARHGEF17
108 clusters sparsely bind to a highly contractile myosin network. In the edge distal lamella
109 region, that is characterized by low contractility, ordered ARHGEF17 cluster arrays
110 bind to transverse arcs, leading to disassembly of myosin filaments through their
111 fracture. ARHGEF17 knockdown (KD) leads to lack of lamella disassembly, impeding
112 symmetry breaking and polarization during spreading. On time scales of multiple
113 hours, this leads to a very contractile stress fiber network. Optogenetic perturbation of
114 contractility dynamics reveals that ARHGEF17 preferentially binds actomyosin
115 networks in a relaxation state. As control cells, *ARHGEF17* KD cells still display a
116 focused RhoA activity pattern at the edge, that has been shown to regulate lamellar
117 contractility (Martin et al., 2016, 2014) . However, decreased RhoA activity is observed
118 at the back of this region, leading to lack of its disassembly. We propose that
119 ARHGEF17 senses ATP-actin at barbed ends of actin filaments within the actomyosin
120 lattice that is disassembling within the low contractile edge distal lamella. This locally
121 activates RhoA-mediated actomyosin contractility that leads to fracture rather than
122 reinforcement re-inforcement of the low contractile lamella, ensuring its efficient
123 disassembly.

124

125

126 **Results**

127

128 **ARHGEF17 binds to the edge distal region of the lamella during spreading**

129

130 To study feedback from the cytoskeleton to Rho GTPases, we evaluated the
131 subcellular localization of multiple GEFs and GAPs that were previously found to bind
132 to F-actin or adhesion structures in REF52 fibroblasts (Müller et al., 2020). Confocal
133 imaging of an exogenously-expressed GFP-tagged version of ARHGEF17
134 simultaneously together with F-actin staining, revealed that ARHGEF17 binds to the
135 edge distal lamella region, as well as to low F-actin containing contractile structures
136 in the middle of the cell (Figure 1B). Spinning disk confocal time-lapse imaging of
137 ARHGEF17 and MLC dynamics during cell spreading again revealed a similar pattern
138 (Figure 1C, Movie S1). Consistently with the fact that ARHGEF17 bears an actin
139 binding domain (Mitin et al., 2012), it displayed retrograde flow together with MLC
140 (Movie S1). Within the central domain of the cell, ARHGEF17 dynamically interacts
141 with a contractile F-actin network with low MLC signal. Kymograph analysis revealed
142 that the lamella exhibited two zones: a discrete band of strong MLC proximally to the
143 edge, and a band of lower MLC signal distally to the edge that exhibits a sharp
144 boundary where the transverse arcs disassemble (Figure 1C, separated by yellow
145 dotted lines). ARHGEF17 displayed a strikingly different pattern: absence of signal in
146 the lamellipodium with an increasing gradient that peaks in the low MLC edge proximal
147 region, at the region where disassembly of transverse arcs occurs. These specific
148 MLC and ARHGEF17 domains remain constant over time (Figure 1C). These data
149 reveals a dynamic ultrastructure of the lamella with regions in which the myosin lattice
150 adopts different densities, with ARHGEF17 prominently binding the edge distal region
151 with low MLC density where lamella disassembly occurs.

152
153 **ARHGEF17 oligomerizes in cluster arrays that correlate with different**
154 **actomyosin networks**
155
156 To better understand ARHGEF17 subcellular localisation within the lamella, we
157 imaged ARHGEF17 and MLC dynamics using structured illumination microscopy
158 (SIM). SIM's enhanced resolution revealed discrete ARHGEF17 punctate structures
159 of different fluorescence intensities that we refer to as clusters, which might involve
160 ARHGEF17 oligomerization through the C-terminal propeller domain (Mitin et al.,
161 2012) (Figure 2A). Most likely through ARHGEF17's actin binding domain, these
162 clusters colocalized with actomyosin structures, and assembled into higher order
163 arrays of clusters (Figure 2A-C). SIM resolved single myosin II filaments and their
164 arrangement as stacks (Hu et al., 2017; Quintanilla et al., 2023) (Figure 2B, Movie
165 S2). We then used an implementation of the Crocker-Grier centroid-finding algorithm
166 (Crocker and Grier, 1996) to locate and quantify blobs that represent the myosin
167 filament heads (Quintanilla et al., 2023) and the ARHGEF17 clusters, and measured
168 distances between the latter (Figure S1A). Quantification of the distance between
169 neighboring myosin filament heads, over the whole cell, revealed a distance of
170 approximately 280 nm (Figure S1B), as previously observed (Hu et al., 2017;
171 Quintanilla et al., 2024, 2023). ARHGEF17 clusters displayed a similar distance
172 distribution (Figure S1B). The distance between neighboring myosin filament heads
173 and ARHGEF17 clusters was 190 nm, suggesting that ARHGEF17 binding to F-actin
174 positions them closely to the myosin filament heads (Figure S1B).
175 We then observed that the retrogradely flowing ARHGEF17 clusters displayed distinct
176 organization patterns that correlated with different spatial arrangements of the
177 actomyosin lattice. We first describe the different subcellular domains with specific

178 actomyosin lattice arrangement. As expected, myosin II filaments were mostly absent
179 from the lamellipodium (Figure 2B,C,D inset 1). In the edge proximal lamella region, a
180 band of high density interwoven network of myosin filaments was observed (Figure
181 2D, inset 2). This crosslinked network most likely emerges from myosin redistribution
182 to the branched lamellipodial actin that condenses into actin arcs (Burnette et al.,
183 2011). Further within the cell, in the edge distal lamella region, we observed a second
184 network of parallel myosin filaments with lower MLC density (Figure 2D inset 3). This
185 explains the subdivision of the lamella in two zones with different MLC densities
186 previously observed with confocal microscopy (Figure 1B,C). Confocal imaging of
187 MLC and pMLC revealed that the edge proximal lamella contained a strong pMLC
188 signal, while the edge distal lamella region contained much lower pMLC signals
189 (Figure 3A,B,C inset 1). High resolution analysis of the edge distal lamella revealed
190 that its parallel myosin arcs are decorated by sparse punctate pMLC puncta (Figure
191 3C inset 2). The cell center was mostly characterized by single myosin filaments that
192 occasionally assemble into arcs, the latter retaining discrete pMLC punta (Figure 3C
193 inset 3). Our blob quantification method revealed that the fluorescence intensities of
194 the MLC signals were higher in the edge proximal versus distal lamella regions, and
195 much lower in the cell center (Figure S1C-E). These results reveal that the lamella
196 contains two separate myosin networks: 1. in the edge proximal lamella region, the
197 myosin network adopts a highly interwoven structure and is under tension with high
198 phosphorylated MLC, 2. the edge distal lamella region consists of a network of linear
199 myosin filaments with mostly low tension. Here the myosin filaments's motor domain
200 might be trapped in a rigor state, and only act as a crosslinker without generation of
201 contractility.

202 Evaluation of ARHGEF17 signals in these different subcellular regions revealed that
203 ARHGEF17 forms arrays of clusters that exhibit increasing fluorescence intensities as
204 they are transported retrogradely (Figure 2D). Small ARHGEF17 puncta were
205 observed in the lamellipodium (Figure 2D, inset 1). In the edge proximal lamella region,
206 ARHGEF17 assembled into larger clusters that localized in between the crosslinked
207 myosin filaments (Figure 2D, inset 2). In the edge distal lamella region, ARHGEF17
208 clusters displayed a further increase in density and formed lattices that are parallel to
209 the myosin filament network (Figure 2D, inset 3). ARHGEF17 clusters form networks
210 suggesting that they bind multiple actin filaments simultaneously (Figure 2D, inset
211 3). Both myosin filaments and ARHGEF17 clusters defined a sharp boundary
212 between the low contractile lamella region and the cell center (Figure 2C, dotted line).
213 In the cell center, we observed homogeneous distribution of ARHGEF17 clusters of
214 lower intensity than those observed in the edge distal lamella (Figure 2D, inset 4).
215 Quantification of fluorescence intensities in detected blobs revealed that ARHGEF17
216 clusters in the contractile edge proximal have lower fluorescence intensity than those
217 present in the low-contractile lamella region and the cell center (Figure S1C-E). We
218 also evaluated the subcellular localization of ARHGEF17 with respect to F-actin and
219 the actin crosslinker α-actinin (Figure 3D-F) using confocal microscopy. In the
220 contractile edge proximal lamella region, α-actinin mostly bound to adhesions and
221 diffuse ARHGEF17 signal were observed (Figure 3F inset 1). In the low contractile
222 edge distal lamella region, we observed that ARHGEF17 clusters were colocalizing
223 with F-actin filaments but were mutually exclusive with α-actinin puncta where F-actin
224 filaments are crosslinked (Figure 3F inset 2). This is consistent with the ability of
225 ARHGEF17 to bind ATP-actin, mostly at the barbed-end (Mitin et al., 2012). We
226 summarize the interactions of ARHGEF17 with the actomyosin lattice in Figure S2.

227
228 **ARHGEF17 clusters flow with the retrograde actin flow and correlate with**
229 **disassembly of actomyosin transverse arcs in the lamella**
230
231 Timelapse SIM imaging revealed that ARHGEF17 clusters flowed back with the actin
232 retrograde flow (Figure 4A,B, Movie S2 and S3). During this process, we observed
233 that the transported ARHGEF17 clusters exhibited fission and fusion events (Figure
234 4A,B, Movie S3), and increased in fluorescence intensity while they are transported
235 back (Figure S1D,E). The correlation of ARHGEF17 transport by the actin retrograde
236 flow, and the formation of ARHGEF17 clusters of increasing fluorescence intensities
237 while transported centripetally strongly suggests a mechanism of advection that leads
238 to coalescence of ARGEF17 into clusters. This flow was interrupted by disassembly
239 of the myosin filament lattice in the lamella edge that faces the center of the cell (Figure
240 4C, Movie S4). An additional confocal timelapse dataset documents how ARHGEF17
241 enrichment correlates with transverse myosin arc disassembly (Figure S3, Movie S5).
242 The high density of myosin arrays in the contractile edge proximal lamella region
243 (Movie S3, upper panels) did not make it possible to quantify if a similar phenomenon
244 occurs at this location. To further quantify the dynamic self organization properties of
245 MLC and ARHGEF17, we evaluated the local correlation of the orientation of
246 fluorescent signals using a custom algorithm inspired by the orientationJ plugin
247 (Püspöki et al., 2016). This was performed for both channels independently. We
248 observed that while the myosin lattice exhibited aligned arcs throughout the lamella,
249 the characteristic aligned ARHGEF17 arrays were mostly observed in the edge distal
250 lamella part at sites where transverse actomyosin arcs disassemble (Figure 4D, Movie
251 S6). In the cell center, small ordered myosin arcs interacted with ARHGEF17 clusters
252 which led to their immediate disassembly (Figure 4E). These datasets suggest the

253 actomyosin retrograde flow dynamically organizes the advection and coalescence of
254 ARHGEF17 clusters to concentrate the latter in transverse actomyosin arcs in the non-
255 contractile lamella. This can also occur on actomyosin arcs transiently occurring in the
256 cell center. When this spatially organizing mechanism of ARHGEF17 concentration
257 exceeds a specific threshold, ARHGEF17 might activate the RhoA-Rho associated
258 protein kinase (ROCK)-MLC activation to locally fracture the low contractile transverse
259 arcs leading to their disassembly. Thus, local activation of RhoA through this spatially
260 organizing mechanism might lead to an opposite effect than reinforcement of
261 contractility which is usually the expected output of the Rho/ROCK pathway.

262

263 **ARHGEF17 loss of function leads to loss of actomyosin disassembly**

264

265 To further evaluate ARHGEF17's function, we performed RNA interference KD
266 experiments, and evaluated F-actin, MLC phosphorylation and focal adhesion outputs
267 during REF52 spreading (Figure 5A). We observed a KD efficiency of 88 % at mRNA
268 level (Figure S4). To quantify these datasets, we built an image analysis pipeline to
269 automatically segment cells and measure fluorescence intensity as a function of
270 distance to the cell border (depicted in Figure S5A,B, see intensity profile analysis in
271 methods section). During cell spreading, *ARHGEF17* KD cells displayed a prominent
272 increase in F-actin signals in the edge distal lamella region (Figure 5A,B). This was
273 accompanied by robust increase in focal adhesion size and intensity, which are
274 hallmarks of high contractility. Surprisingly, this phenotype was only accompanied by
275 a modest increase in phosphorylated pMLC given these robust contractile responses
276 (Figure 5B). Time-lapse imaging of F-actin dynamics of *ARHGEF17* KD cells starting
277 from the onset of cell spreading revealed that the latter remain spread longer than their
278 control counterparts (Figure 5C, quantified in Figure 5D - area measurements, Movie

279 S7). Further, *ARHGEF17* KD cells lacked the ability to break symmetry much longer
280 than control cells, despite displaying a more contractile cytoskeleton (quantified in
281 Figure 5D - solidity measurements). Approximately 12 hours after initial spreading, we
282 observed that *ARHGEF17* KD cells display a very contractile actomyosin network with
283 respect to their control counterparts (Figure 5C - 12 hours). To better understand the
284 nature of the increased tension in the lamella cytoskeletal network in response to
285 *ARHGEF17* KD, we imaged MLC using SIM. We observed increased stacking of
286 myosin filaments in *ARHGEF17* KD cells in both the edge proximal and edge distal
287 lamella, with the density of myosin filaments decreasing in the edge distal lamella
288 region for both conditions (Figure 5E, quantified in Figure S5C). These results reveal
289 that loss of function of the RhoA-specific GEF ARHGEF17, leads to loss of actomyosin
290 disassembly in the edge distal non-contractile lamella. This leads to high contractility,
291 as observed at the level of F-actin and focal adhesions, in presence of only a small
292 increase in pMLC. After initial spreading, *ARHGEF17* KD cells display strong and
293 exceptionally stable contractile arcs which might explain the lack of the ability to break
294 symmetry for cell polarization. After multiple hours, *ARHGEF17* KD cells display an
295 extremely contractile actomyosin network. SIM imaging reveals that *ARHGEF17* KD
296 cells display increased stacking of myosin filaments. Together with the finding that
297 ARHGEF17 recruitment to the actomyosin lattice leads to its disassembly (Figure 3),
298 these results indicate that ARHGEF17 regulates disassembly of actomyosin networks
299 in the non contractile edge distal lamella.
300
301 **ARHGEF17 loss of function decreases RhoA activity in the edge distal lamella**
302
303 To evaluate how ARHGEF17 spatio-temporally regulates RhoA, we evaluated the
304 effect of ARHGEF17 loss of function on RhoA activation patterns as measured by the

305 FRET biosensor RhoA2G (Fritz et al., 2013). We simultaneously imaged F-actin
306 dynamics using the lifeact construct. In spreading REF52 cells, we observed that as
307 previously described (Martin et al., 2016, 2014), RhoA activity displays a focused
308 region of RhoA activity directly at the leading edge, of similar size than the
309 lamellipodium and the contractile edge proximal lamella as observed in Figure 3A-C
310 (Figure 6, Movie S8). This was followed by a zone of lower RhoA activity (Figure 6A).
311 As observed in figure 5A, *ARHGEF17* KD cells displayed an intense F-actin signal in
312 the edge distal lamella, due to lack of their disassembly. In these cells, the edge
313 localized RhoA activity pool remained unchanged, but lower RhoA activity correlated
314 with lack of F-actin network disassembly in the edge distal lamella (particularly visible
315 in the kymographs in figure 6B). Quantification by radially averaging RhoA activity
316 across the periphery of the cell (Figure 6C,D) revealed that the RhoA activity pool at
317 the edge remained unchanged, while the RhoA activity pool in the edge distal lamella
318 is lower in perturbed versus control cells. Global RhoA activity levels did not change
319 between control and perturbed cells, indicating that a very small pool of RhoA activity
320 is affected by *ARHGEF17* KD (Figure 6E). The finding that both RhoA activity (Figure
321 6) and pMLC signals (Figure 5) remain present in the edge proximal lamella in
322 *ARHGEF17* KD cells strongly suggests that this specific RhoA activity pool regulates
323 lamellar contractility. The low contractile edge distal lamella might then emerge
324 through retrograde flow in absence of RhoA/ROCK mediated MLC phosphorylation.
325 The finding of lower RhoA activity in the edge distal lamella, that correlates with
326 absence of F-actin network disassembly, indicates that ARHGEF17 regulates this
327 specific RhoA activity pool. Thus, two spatio-temporal RhoA activity pools, one in the
328 edge proximal and one in the edge distal lamella exist, and regulate actomyosin
329 assembly and disassembly respectively.

330
331 **ARHGEF17 preferentially binds to relaxing actomyosin networks**

332
333 The striking localisation of ARHGEF17 at myosin arcs, especially in the edge distal
334 low contractile lamella, strongly suggests that ARHGEF17 binds to relaxed,
335 disassembling myosin arcs (Figure 4). To test this hypothesis with an orthogonal
336 approach, we used an optogenetic system to locally transiently activate Rho to evoke
337 a temporary pulse of contractility followed by relaxation, and evaluate resulting
338 ARHGEF17 dynamics. We used a re-engineered optoLARG actuator consisting of a
339 nano SspB domain for efficient light-dependent recruitment of the LARG GEF domain
340 to the iLID domain that was fused to a slowly diffusing stargazin membrane anchor
341 (Heydasch et al., 2023) (Figure 7A). This construct was stably expressed at low levels
342 together with ARHGEF17-mCherry and lifeact-miRFP F-actin (Figure 7A). Illumination
343 of a spot with blue light led to local contractility as evidenced by accumulation of F-
344 actin (Figure 7B, Movie S9). After blue light removal, contractility rapidly disappeared.
345 Kymograph analysis revealed that ARHGEF17 was specifically binding to relaxing
346 actomyosin networks. To further corroborate this finding, we imaged ARHGEF17
347 dynamics in response to myosin network relaxation triggered by Y-27632-mediated
348 ROCK inhibition (Figure 7C, Movie S10). We found that after ROCK inhibition,
349 ARHGEF17 was immediately recruited to the relaxing actomyosin network until it
350 eventually completely disassembled. Together, these results strengthen the idea that
351 ARHGEF17 selectively binds to actomyosin arrays that are in a state of relaxation.

352 **Discussion**

353 While assembly of contractile actomyosin systems has been extensively studied, their
354 disassembly remains virtually unexplored. It is currently assumed that cessation of

355 Rho/ROCK signaling, which leads to activation of myosin light chain phosphatase
356 (Amano et al., 2010) is sufficient for actomyosin network disassembly. Here, we report
357 on a spatio-temporal signaling system dedicated to lamella disassembly. We show
358 that ARHGEF17's recruitment to the low contractile, edge distal region of the lamella,
359 locally activates RhoA, and leads to its disassembly (Figure 8). This challenges the
360 commonly accepted notion that RhoA solely regulates actomyosin network assembly,
361 and shows that it can also control its disassembly. This underscores the need to
362 understand Rho GTPase signaling in time and space and is consistent with the
363 hypothesis of spatio-temporal signaling modules in which one GTPase can be spatially
364 controlled by specific GEFs and GAPs to perform different functions in time and space
365 (Pertz, 2010). A model on how ARHGEF17 regulates the disassembly of the lamellar
366 actomyosin network is depicted in Figure 8.
367
368 An important component of this spatio-temporal signaling system is the mechanism
369 by which ARHGEF17 is dynamically recruited to the lamella back region. SIM imaging
370 of myosin networks and ARHGEF17 dynamics indicate that ARHGEF17 is transported
371 backward with the actin retrograde flow (Figure 4A,B). This must involve the N-terminal
372 domain of ARHGEF17 that shows high selectivity for ATP-actin, and thus barbed ends
373 of F-actin filaments within the actomyosin lattice (Mitin et al., 2012) (Figure 8A). We
374 observe that during this process ARHGEF17 clusters form through fusion-fission
375 events (Figure 4A,B) and grow in size while they are transported centripetally (Figure
376 2, quantified in Figure S1C-E). This ultimately leads to highest ARHGEF17 density on
377 linear transverse arcs in the edge distal lamella where the latter disassembles (Figures
378 2, 4C, S2, Movies S3-S4). Formation of ARHGEF17 clusters most likely involve the
379 C-terminal β-propeller domain (Mitin et al., 2012), a domain regulating oligomerization
380 in multiple proteins such as clathrin (Wood and Smith, 2021) or Cdc20 and Cdh1 that

381 are involved in the activation of the anaphase-promoting complex/cyclosome during
382 cell division (Peters, 2006). The observation that ARHGEF17 clusters bear similar size
383 features than myosin filaments (Figure S1B), strongly suggest that these clusters
384 contain tens of ARHGEF17 molecules. Our live imaging data suggests that
385 ARHGEF17 clusters grow through an advection mechanism that involves interaction
386 with F-actin filaments during retrograde flow. Note that ARHGEF17 also contains a
387 PH domain that has been documented to bind to membranes (Mitin et al., 2012).
388 Confining ARHGEF17 transport to the membrane might feed into this advection
389 mechanism. An open question is why ARHGEF17 does not efficiently bind actin
390 barbed ends in the lamellipodium. We speculate that interactions with F-actin together
391 with the advection mechanism are necessary for concentration of ARHGEF17 clusters
392 in the back lamella region. Once ARHGEF17 clusters disassemble together with the
393 transverse myosin arcs in the distal lamella, they persist as disordered clusters in the
394 cell center (Figure 2D, quantified in Figure S1C-E) where they control disassembly of
395 spurious actomyosin networks in the cell center (Figure 4C).
396
397 Another important aspect of our spatio-temporal signaling system is how ARHGEF17
398 leads to actomyosin network disassembly during cell spreading. As just mentioned
399 above, ARHGEF17 interactions allow its dynamic accumulation at the lamella back
400 region where it correlates with actomyosin network disassembly (Figure 4).
401 ARHGEF17 KD experiments (Figure 5) as well as FRET experiments indicated that
402 ARHGEF17 regulates actomyosin disassembly through a RhoA-dependent
403 mechanism (Figure 6). How does this work ? We propose that local application of
404 tension through ARHGEF17/RhoA/ROCK might fracture transverse arcs in the lamella
405 back leading to their disassembly. This is consistent with *in vitro* (Murrell and Gardel,
406 2012) and *in vivo* (Wilson et al., 2010) evidence that myosin contractility can

407 disassemble actin networks. This mechanism might be further influenced by the
408 following factors: 1. Build-up of robust ARHGEF17 clusters might allow for a critical
409 concentration of local ARHGEF17 to efficiently locally switch ON RhoA activity; 2. the
410 position of ARHGEF17 clusters at the barbed end of F-actin filaments, away from α-
411 actinin mediated crosslinks which are crucial for stability of actomyosin networks
412 (Dwyer et al., 2022), might be an advantageous weak point to fracture the transverse
413 myosin arcs through local application of tension (Figure 8); 3. prominent ARHGEF17
414 clusters specifically localize within the low contractile edge distal lamella in which
415 myosins might only act as crosslinkers, which might be easier to fracture (Figure 8B);
416 4. low contractile actomyosin networks in the edge distal lamella might already be
417 prone to disassembly, producing new barbed ends for actin polymerization, ATP-actin
418 incorporation, and thus further ARHGEF17 recruitment. Our optogenetic and drug
419 perturbations of contractility (Figure 7) specifically illustrate the last point - during an
420 optogenetically-evoked contractility transient, ARHGEF17 specifically binds to
421 relaxing actomyosin networks (Figure 7A,B). Here, disassembling myosin networks
422 might produce barbed ends that can incorporate ATP-actin, and recruit ARHGEF17
423 that provides a positive feedback by locally and transiently evoking RhoA-mediated
424 contractility. An identical scenario applies to our ROCK inhibition studies (Figure 7C).
425 Thus, the self-organization properties of ARHGEF17, that involve interaction with
426 ATP-actin at F-actin barbed ends, as well as oligomerization might allow for its
427 localization to low contractile, disassembling myosin networks at the lamella back
428 region, providing a positive feedback for their robust disassembly.
429
430 Our data reveals the existence of two spatially distinct RhoA activation zones at the
431 leading edge of the cell, the 1st regulating actomyosin assembly, and the 2nd
432 regulating actomyosin disassembly. The 1st spatial pool of RhoA activity spans the

433 lamellipodium and the contractile edge proximal lamella region, displays high pMLC
434 signals (Figure 3A-C) and regulates actomyosin network assembly as already shown
435 before (Martin et al., 2016, 2014). Rac1 activity is also present at that location (Martin
436 et al., 2016), and RhoA activity might locally apply tension to lamellipodial branched
437 actin network to switch on actomyosin retrograde flow. The finding that *ARHGEF17*
438 KD maintains the 1st spatial pool of RhoA (Figure 6) indicates that another GEF and
439 GAP must regulate it. Candidate RhoA-specific GEFs might be LARG and GEF-H1
440 that have been shown to regulate cytoskeletal responses in response to force
441 application to integrins (Guilluy et al., 2011). The precise mechanisms that shape this
442 focused RhoA activity pool remain to be discovered. The second ARHGEF17-
443 mediated spatial RhoA activity pool is less intense and spans the non-contractile edge
444 distal lamella region that displays sparse pMLC signals to regulate contractility for
445 actomyosin network disassembly. Through retrograde flow, the contractile actomyosin
446 network under tension in the 1st zone transitions in the 2nd zone of low RhoA activity,
447 and adopts a relaxed state in which myosin filaments only displaying sparse pMLC
448 signals, and thus most likely only acting as crosslinkers. This poorly disassembling
449 actomyosin network can then activate ARHGEF17-mediated contractility through the
450 mechanisms we have discussed above. Thus, there are two specific RhoA spatio-
451 temporal activity pools that are regulating the lamella through different self-
452 organization logics, with the ARHGEF17-regulated pool specifically dedicated for
453 disassembly of actomyosin networks. Note that these RhoA activity patterns are
454 particularly difficult to spatially resolve simply because active RhoA diffuses in the
455 plasma membranes by virtue of its C-terminal geranylgeranyl moiety. Consequently,
456 it is not possible to visualize ARHGEF17-mediated local MLC activation occurring at
457 barbed ends in the low contractile edge-distal lamella. A better understanding of these

458 different spatio-temporal RhoA activity pools will require single molecule imaging
459 methods that have been previously used to image Rho GTPase dynamics (Mehidi et
460 al., 2019).
461
462 Our work exemplifies the function of spatio-temporal feedback regulation in Rho
463 GTPase signaling. Such feedback regulation is ubiquitous in Rho GTPase signaling,
464 and for now has been mostly shown to be responsible for shaping spatio-temporal
465 signaling patterns (Bement et al., 2024). In our work, the ARHGEF17 pathway can be
466 understood as a spatially-regulated positive feedback to ensure robust and irreversible
467 disassembly of actomyosin networks. This might be required for efficient homeostasis
468 of the actomyosin cytoskeleton warranting the absence of contractile instabilities that
469 might lead to actomyosin network buckling, fracturing, or the formation of aggregates
470 as observed in cell free systems (Ideses et al., 2018). Further illustrating the concept
471 that Rho GTPase feedback mechanisms are important for cellular homeostasis, we
472 have recently observed a similar positive feedback mechanism impinging on RhoA
473 activity that involves spatio-temporal regulation of the RhoGAP DLC1 at focal
474 adhesions (Heydasch et al., 2023). Here, the positive feedback emerges from a
475 mechanical input at focal adhesions, which locally amplifies RhoA signaling, and is
476 required for irreversible focal adhesion disassembly. The finding that 30% of Rho
477 GEFs/GAPs bind to the cytoskeleton or adhesions (Müller et al., 2020) strongly
478 suggests widespread mechanisms of cytoskeletal to Rho GTPase feedback that might
479 regulate cytoskeletal homeostasis or Rho GTPase pattern formation (Bement et al.,
480 2024). Future elucidation of the role of GEFs and GAPs in spatio-temporal Rho
481 GTPase signaling will need to take into account the concept of feedback regulation.
482
483

484 **ONLINE METHODS**

485 **Cell Culture and Transfection**

486
487 Rat Embryo Fibroblast 52 (REF52) cells were cultured in Dubelcco's Modified Eagle
488 Medium with 4.5 g/L glucose, 10% 4mM L-Glutamine, and 100 U/mL
489 penicillin/streptomycin. Cells were grown at 37ºC and 5% CO2.
490 For transfection, REF52 cells (45000 per well) were seeded in a 6-well plate a day
491 before. Cells were transfection using Lipofectamine 3000 Reagent and following the
492 protocol (Thermo Fisher). Transfected cells were kept overnight and visualised the
493 next day.
494

495 **siRNA KD**

496
497 4 ul of Lipofectamine RNAiMax (Thermo) was added to 500 ul of Opti-MEM (Thermo)
498 and siPOOL solution for 3 nM final siRNA concentration. This mix was added to a well
499 of 6-well plate and reverse transfection was done by adding 120000 cells in 1.5 mL
500 medium volume in the well. After 24 hours, cells were re-seeded on glass bottom well
501 plates (Celvis) which were coated with 5 µg/ml of human plasma fibronectin purified
502 protein.
503
504 **DNA constructs**

505
506 The optoLARG construct used was: pB3.0-optoLARG-mVenus-SspB-p2A-stargazin-
507 mtq2-iLID, as described in Heydasch et al., 2023. ARHGEF17-mCherry construct was
508 provided by Olivier Rocks, and ARHGEF17-GFP construct was from addgene #58893.
509 MLC-mCherry, MLC-miRFP, LifeAct-miRFP and LifeAct-mNeonGreen were prepared
510 previously in the lab.

511
512 **Optogenetic Experiments**

513
514 REF-52 cells with optoLARG construct and LifeAct-miRFP were transfected with
515 ARHGEF17-mCherry (kindly provided by Olivier Rocks) and plated on glass bottom
516 well plates (Celvis) which were coated with 5 µg/mL of human plasma fibronectin
517 purified protein (Merck) for one hour at room temperature. Cells were seeded at 6000
518 cells/well into 12 well plates and allowed to attach for 12 hours. Before imaging,
519 FluoroBrite DMEM medium was added to the cells. NIS-Elements (Nikon) was used
520 on the microscope for observing ARHGEF17 and LifeAct dynamics. Optogenetic
521 stimulation was localized to specific regions using an Andor mosaic 3 DMD and the
522 ROIs were individually defined for the cells. The images were taken using a 60x oil
523 objective. mCherry-ARHGEF17 and miRFP-LifeAct were imaged for 20 cycles with 5
524 seconds time interval for baseline, then stimulation with blue light in the ROI for 65
525 cycles with 5 seconds time interval, followed by no stimulation acquisition with 5
526 seconds time interval.

527

528 **Immunofluorescence antibody staining**

529
530 Vinculin, pMLC, Phalloidin-Atto647N (1:200 dilution), Alexa-Fluor-conjugated
531 secondary antibodies (used as 1:1000) were from Molecular Probes. One hour after
532 seeding, cells were fixed with 0.2% cold paraformaldehyde for 10 min, washed with
533 1x PBS three times, permeabilized with 0.1% Triton X solution, washed again with 1x
534 PBS, and blocked for 30 min at RT with 2% BSA solution in PBS. Cells were incubated
535 overnight with the primary antibody, and then washed with 2% BSA solution in PBS
536 three times next day. Secondary antibody incubation was done for 1 hour at RT
537 followed by three washes with 1x PBS.

538

539 **Y-27632 washout experiment**

540

541 REF-52 cells with LifeAct-miRFP were transfected with ARHGEF17-mCherry and
542 seeded on a 24-well glass bottom plate coated with 5 µg/mL fibronectin. Cells were
543 allowed to attach for 12 hours and FluoroBrite DMEM medium was added later for
544 imaging. Live cell imaging was done for addition of Y-27632. mCherry-ARHGEF17
545 and miRFP-LifeAct were imaged for 20 cycles with 5 seconds time interval for baseline
546 and then 32 µm of Y-27632 was added. Imaging was continued with 5 seconds time
547 interval until complete disassembly of actomyosin.

548

549 **RNA Extraction**

550

551 Cells growing in a 6-well plate were rinsed with PBS and 1 mL TRI-Reagent per well
552 was added. After 3 minutes of incubation, cells were transferred to a 15 mL tube and
553 200 µL chloroform was added. The tube was vortexed for 30 seconds and kept
554 standing for 5 min at RT. After this it was centrifuged at maximum speed for 5 min in
555 a centrifuge pre-cooled to 4°C. For each sample, 2 µL glycogen (20 mg/mL) was
556 pipetted in fresh eppendorf tubes. From the centrifuged samples, 350 µL of upper
557 aqueous phase was carefully removed and transferred into the corresponding tube
558 containing glycogen. 600 µL of isopropanol was then added to each tube and mixed
559 by inversion. The tubes were kept for 10 min at RT and then centrifuged at 4°C at
560 maximal speed for 15 min. The supernatant was carefully removed and discarded.
561 The pellet was gently rinsed with 1 mL ethanol 80% (diluted with DEPC water). The
562 tube was centrifuged for 5 min at maximal speed and supernatant was discarded. The
563 pellet was left to dry for 15 min and then 40 µL DEPC water was used to dissolve the

564 pellet. The extracted RNA was kept on ice and concentration measured in a Nanodrop
565 spectrophotometer.
566
567 **Reverse Transcription and qPCR**
568
569 To reverse transcribe all polyadenylated mRNAs of a cell an oligo(dT) primer can be
570 used which hybridises to the poly(A) tails of the mRNAs. For primer annealing, for
571 each reaction, 5µg RNA + 1µl oligo (dT) primer 10µM were mixed and filled up to total
572 25 µl with water. This was incubated for 5 min at 75°C and then let stand at RT for 5
573 min. 25 µl of 2X reverse transcription complementation mix was prepared for each
574 sample. For 25 µl 2X RT mix, 10.9 µl H2O, 5 µl 10X Affinity-ScriptTM buffer, 5 µl 100
575 mM DTT, 2.5 µl dNTP Mix 10 mM each from NEB, 0.8 µl RNAse inhibitor (Dundee
576 Cell Products) and 0.8 µl Reverse Transcriptase (Affinity Script Kit,
577 Agilent/Stratagene) were mixed. The 25 µl 2X RT mix was added to each sample with
578 RNA and annealed oligo(dT) primer, total 50 µl per tube. This was incubated for 10
579 min at 25°C (primer extension), 40 min at 42°C (reverse transcription) and 20 min at
580 60°C (enzyme inactivation). The resulting cDNA can be stored at -20°C. For qPCR,
581 following primer pairs were used. GAPDH Fwd: GTCTCCTCTGACTTCAACAGCG,
582 GAPDH Rv: ACCACCCTGTTGCTGTAGCCAA, ARHGEF17 Fwd:
583 CATAGCTTCTCCCAACCGCA, ARHGEF17 Rv: AGGTACGCAGGAAAGCTCAC.
584 For 20 µl reaction, 10 µl of SYBR™ Green PCR Master Mix 1X (Thermo Fisher), 0.4
585 µl each of 10 mM Fwd and Rv primers, 15 ng of cDNA and water upto 20 µl were
586 mixed and added to qPCR plate. Following program was run: Enzyme activation at 95
587 °C 1 min (1 cycle), Denature at 95 °C during 3 sec, Anneal/Extend/Acquire at 60 ºC
588 15 sec. 40 cycles were done and data analysed.
589

590 **Structured illumination microscopy (SIM)**

591 8-well chambered slides (Ibidi) coated with 5 µg/mL fibronectin were used for live cell
592 imaging using SIM. REF-52 cells with MLC-mCherry were transfected with
593 ARHGEF17-GFP (addgene #58893) and seeded in 8-well chambered slide. 30 min
594 after seeding, FluoroBrite DMEM medium was added and cells were imaged using
595 63x oil objective using 488 and 561 laser. The interval time between images is
596 30 seconds. The processing of the acquired data was done using Zen 3.0 imaging
597 software. The SIM Imaging was done at the Center for Microscopy and Image Analysis
598 at the University of Zürich.

599 **RhoA activity FRET imaging**

600 8-well chambered slides were coated with 5 µg/mL fibronectin. REF52 cells were
601 seeded in Fluorobrite DMEM supplemented with 0.5% FBS, 0.5% BSA, L-glutamine
602 and P/S. After 1 h images were acquired on a Nikon Eclipse Ti inverted microscope
603 with a 60x Plan Apochromat Objective, using a Prim95B sCMOS camera with 2x2
604 pixel binning.

605 Donor and FRET channels were excited using a Lumencor Spectra X 440 nm LED
606 and imaged sequentially with excitation filters 430/24 and a Dichroic Q465 long-pass
607 filter. For donor emission, a 480/40 nm bandpass filter was used, and for FRET
608 emission, a 535/30 nm bandpass filter was used.

609 Data was analyzed with custom python code with the pipeline described in (Spiering
610 et al., 2013).

611 **Image analysis**

Standard Python libraries were used for data processing and visualization (NumPy 1.24.4, pandas 2.0.3, skimage 0.22.0, Matplotlib 3.8.2).

SIM cluster analysis (Figure S1 and S4C)

For the analysis of clusters in SIM images in Figures 2 and 5, blob-like structures were detected using the Crocker-Grier centroid-finding algorithm (Crocker and Grier, 1996) implemented in the Python library Trackpy (version 0.6.1, https://zenodo.org/records/7670439). The expected diameter was set to 3 pixels, and the image was inverted to match the input format expected by Trackpy. For the distance analysis, nearest neighbors were detected by constructing and parsing a KD tree, using the algorithm described in (Maneewongvatana and Mount, 1999), which is implemented in the Python library SciPy version 1.9.1 (Virtanen et al., 2020).

Linear structure enhancement and orientation analysis (Figure 4D,E)

Linear structures and their orientations were detected by convolving the image with a 2D Gabor filter bank (Granlund, 1978). For all pixels, the vector pointing towards a manually placed cell centroid was calculated, and the orientation was derived as an angle from this vector. This angle was then compared to the angle of the Gabor filter with the highest response. Aligned angles (more pointing towards the cell center) were colored in blue, while non-aligned angles (more parallel to the cell edge) were colored in red. Final visualization was done using an HSI (hue, saturation, intensity) model inspired by the software OrientationJ (Püspöki et al., 2016). The blue/red values were used as hue, the Gabor filter response as saturation, and the original image as intensity values. The code to reproduce the figure is available on github as a Jupyter notebook (https://github.com/hinderling/orientation-py).

Intensity profile analysis (Figure 5B)

Cells were segmented with Cellpose (Stringer and Pachitariu, 2024) using the cyto3 model, a diameter of 150 px, and Phalloidin and DAPI as input channels. Cells touching the image border were excluded from the analysis. A Euclidean distance transform was applied to the cell masks to find the distance from the cell border for each pixel. For each cell, pixels with the same distance were binned, and the mean intensity was calculated for all background-subtracted fluorescence channels. The first 60 pixels (~20 µm) were chosen for plotting. Cells with a shorter maximal distance were excluded from further analysis (mean maximal distance for all cells was 69.56 px).

Statistics

Statistics were computed with scipy (version 1.9.1).

Author contributions.

VR and OP conceptualized the paper, VR and BG performed experiments, BG and LH performed data analyses and wrote code, JVU built the optogenetic toolkit, VR and OP wrote the paper.

Acknowledgements.

We thank Daniel Riveline, Karsten Kruse, Damian Brunner and Miguel Vicente-Manzanares for constructive comments on the manuscript. We are grateful to Oliver Rocks for providing constructs, and Judith Trüb for help with cloning. We are grateful to the Microscopy Imaging Center of the University of Bern (https://www.mic.unibe.ch) and the Center for Microscopy and Image Analysis of the University of Zurich (https://www.zmb.uzh.ch) for support. This work was supported by the Swiss National Science Foundation Sinergia grant CRSII5_183550 to OP.

Additional Information

The authors declare no competing interests.

Supplemental Information.

Supplementary Movie legends.

Movie S1: Spinning disc confocal time lapse movie of MLC and ARHGEF17 in a spreading REF52 fibroblast. Scale bar: 10 µm. Time: minutes:seconds.

Movie S2: SIM movie of MLC-mCherry and ARHGEF17-GFP of a spreading REF52 cell. Scale bar: 10 µm. Time: minutes:seconds.

Movie S3: High magnification timeseries insets of ARHGEF17/MLC SIM movie S2 zooming on the edge proximal contractile (top panel corresponding to Figure 4A) and edge distal non contractile (bottom panel corresponding to Figure 4B) lamella. Scale bar: 1 µm. Time: minutes:seconds.

Movie S4: High magnification timeseries insets of ARHGEF17/MLC SIM movie S2, relevant to Figure 4C. Direction of actomyosin flow : Top to bottom. Scale bar: 1 µm. Time: minutes:seconds.

Movie S5: Additional example of MLC-miRFP and ARHGEF17-GFP dynamics during myosin transverse arc disassembly relevant to Figure S2.
Scale bar: 10 µm. Time: minutes:seconds.

Movie S6: Quantification of MLC and ARHGEF17 lattice orientations using orientation-py corresponding to Figure 4D. Scale bar: 10 µm. Time: minutes:seconds.

Movie S7: Epifluorescence time lapse movie of control and ARHGEF17 KD REF52 cells expressing the F-actin marker Lifeact-mNeonGreen. Scale bar = 20 µm. Time hours:minutes.

Movie S8: FRET measurement of RhoA activation and F-actin dynamics in spreading control versus *ARHGEF17* KD REF52 cells. Scale bar = 10 µm. Time hours:minutes.

Movie S9: Optogenetic stimulation of a small ROI in REF52 cells expressing optoLARG, LifeAct-miRFP and ARHGEF17-mCherry. Scale bar = 10 µm. Time minutes:seconds.

Movie S10: ARHGEF17-mCherry and F-actin (LifeAct-mNeonGreen) dynamics before and after relaxation triggered by Y-27632 ROCK inhibition. Scale bar = 20 µm. Time minutes:seconds.

References

1. Amano M, Nakayama M, Kaibuchi K. 2010. Rho-kinase/ROCK: A key regulator of the cytoskeleton and cell polarity. *Cytoskeleton* 67:545–554. doi:10.1002/cm.20472
2. Bement WM, Goryachev AB, Miller AL, von Dassow G. 2024. Patterning of the cell cortex by Rho GTPases. *Nat Rev Mol Cell Biol* 25:290–308. doi:10.1038/s41580-023-00682-z
3. Burnette DT, Manley S, Sengupta P, Sougrat R, Davidson MW, Kachar B, Lippincott-Schwartz J. 2011. A role for actin arcs in the leading-edge advance of migrating cells. *Nat Cell Biol* 13:371–382. doi:10.1038/ncb2205
4. Crocker JC, Grier DG. 1996. Methods of Digital Video Microscopy for Colloidal Studies. *J Colloid Interface Sci* 179:298–310. doi:10.1006/jcis.1996.0217

724 5. Dwyer ME, Robertson-Anderson RM, Gurmessa BJ. 2022. Nonlinear Microscale
725 Mechanics of Actin Networks Governed by Coupling of Filament Crosslinking and
726 Stabilization. *Polymers* 14:4980. doi:10.3390/polym14224980
727 6. Etienne-Manneville S, Hall A. 2002. Rho GTPases in cell biology. *Nature* 420:629–
728 635.
729 7. Fritz RD, Pertz O. 2016. The dynamics of spatio-temporal Rho GTPase signaling:
730 formation of signaling patterns. *F1000Research* 5.
731 doi:10.12688/f1000research.7370.1
732 8. Granlund GH. 1978. In search of a general picture processing operator. *Comput*
733 *Graph Image Process* 8:155–173. doi:10.1016/0146-664X(78)90047-3
734 9. Guilluy C, Swaminathan V, Garcia-Mata R, O'Brien ET, Superfine R, Burridge K.
735 2011. The Rho GEFs LARG and GEF-H1 regulate the mechanical response to
736 force on integrins. *Nat Cell Biol* 13:722–727. doi:10.1038/ncb2254
737 10. Heydasch M, Hinderling L, Van Unen J, Dobrzynski M, Pertz O. 2023. GTPase
738 activating protein DLC1 spatio-temporally regulates Rho signaling.
739 doi:10.7554/eLife.90305.1
740 11. Hu S, Dasbiswas K, Guo Z, Tee Y-H, Thiagarajan V, Hersen P, Chew T-L, Safran
741 SA, Zaidel-Bar R, Bershadsky AD. 2017. Long-range self-organization of
742 cytoskeletal myosin II filament stacks. *Nat Cell Biol* 19:133–141.
743 doi:10.1038/ncb3466
744 12. Ideses Y, Erukhmovitch V, Brand R, Jourdain D, Salmeron Hernandez J, Gabinet
745 U, Safran SA, Kruse K, Bernheim-Groswasser A. 2018. Spontaneous buckling of
746 contractile poroelastic actomyosin sheets. *Nat Commun*.
747 13. Itoh RE, Kurokawa K, Ohba Y, Yoshizaki H, Mochizuki N, Matsuda M. 2002.
748 Activation of Rac and Cdc42 Video Imaged by Fluorescent Resonance Energy

749 Transfer-Based Single-Molecule Probes in the Membrane of Living Cells. *Mol Cell*
750 *Biol* 22:6582–6591. doi:10.1128/MCB.22.18.6582-6591.2002
751 14. Kraynov VS, Chamberlain C, Bokoch GM, Schwartz MA, Slabaugh S, Hahn KM.
752 2000. Localized Rac activation dynamics visualized in living cells. *Science*
753 290:333–337.
754 15. Machacek M, Hodgson L, Welch C, Elliott H, Pertz O, Nalbant P, Abell A, Johnson
755 GL, Hahn KM, Danuser G. 2009. Coordination of Rho GTPase activities during
756 cell protrusion. *Nature* 461:99–103. doi:10.1038/nature08242
757 16. Maneewongvatana S, Mount DM. 1999. Analysis of approximate nearest neighbor
758 searching with clustered point sets. doi:10.48550/arXiv.cs/9901013
759 17. Martin K, Reimann A, Fritz RD, Ryu H, Jeon NL, Pertz O. 2016. Spatio-temporal
760 co-ordination of RhoA, Rac1 and Cdc42 activation during prototypical edge
761 protrusion and retraction dynamics. *Sci Rep* 6:21901. doi:10.1038/srep21901
762 18. Martin K, Vilela M, Jeon NL, Danuser G, Pertz O. 2014. A growth factor-induced,
763 spatially organizing cytoskeletal module enables rapid and persistent fibroblast
764 migration. *Dev Cell* 30:701–716. doi:10.1016/j.devcel.2014.07.022
765 19. Mehidi A, Rossier O, Schaks M, Chazeau A, Binamé F, Remorino A, Coppey M,
766 Karatas Z, Sibarita J-B, Rottner K, Moreau V, Giannone G. 2019. Transient
767 Activations of Rac1 at the Lamellipodium Tip Trigger Membrane Protrusion. *Curr*
768 *Biol* 29:2852-2866.e5. doi:10.1016/j.cub.2019.07.035
769 20. Mitin N, Rossman KL, Currin R, Anne S, Marshall TW, Bear JE, Bautch VL, Der
770 CJ. 2013. The RhoGEF TEM4 Regulates Endothelial Cell Migration by
771 Suppressing Actomyosin Contractility. *PLoS ONE* 8:e66260.
772 doi:10.1371/journal.pone.0066260

773 21. Mitin N, Rossman KL, Der CJ. 2012. Identification of a Novel Actin-Binding
774 Domain within the Rho Guanine Nucleotide Exchange Factor TEM4. *PLoS ONE*
775 7:e41876. doi:10.1371/journal.pone.0041876
776 22. Müller PM, Rademacher J, Bagshaw RD, Wortmann C, Barth C, van Unen J, Alp
777 KM, Giudice G, Eccles RL, Heinrich LE, Pascual-Vargas P, Sanchez-Castro M,
778 Brandenburg L, Mbamalu G, Tucholska M, Spatt L, Czajkowski MT, Welke R-W,
779 Zhang S, Nguyen V, Rrustemi T, Trnka P, Freitag K, Larsen B, Popp O, Mertins
780 P, Gingras A-C, Roth FP, Colwill K, Bakal C, Pertz O, Pawson T, Petsalaki E,
781 Rocks O. 2020. Systems analysis of RhoGEF and RhoGAP regulatory proteins
782 reveals spatially organized RAC1 signalling from integrin adhesions. *Nat Cell Biol*
783 22:498–511. doi:10.1038/s41556-020-0488-x
784 23. Murrell MP, Gardel ML. 2012. F-actin buckling coordinates contractility and
785 severing in a biomimetic actomyosin cortex. *Proc Natl Acad Sci* 109:20820–
786 20825. doi:10.1073/pnas.1214753109
787 24. Nalbant P, Hodgson L, Kraynov V, Toutchkine A, Hahn KM. 2004. Activation of
788 endogenous Cdc42 visualized in living cells. *Science* 305:1615–1619.
789 25. Pertz O, Hodgson L, Klemke RL, Hahn KM. 2006. Spatiotemporal dynamics of
790 RhoA activity in migrating cells. *Nature* 440:1069–1072. doi:10.1038/nature04665
791 26. Peters J-M. 2006. The anaphase promoting complex/cyclosome: a machine
792 designed to destroy. *Nat Rev Mol Cell Biol* 7:644–656. doi:10.1038/nrm1988
793 27. Ponti A, Machacek M, Gupton SL, Waterman-Storer CM, Danuser G. 2004. Two
794 Distinct Actin Networks Drive the Protrusion of Migrating Cells. *Science* 305:1782–
795 1786. doi:10.1126/science.1100533

796 28. Püspöki Z, Storath M, Sage D, Unser M. 2016. Transforms and Operators for
797 Directional Bioimage Analysis: A Survey. *Adv Anat Embryol Cell Biol* 219:69–93.
798 doi:10.1007/978-3-319-28549-8_3
799 29. Quintanilla MA, Hammer JA, Beach JR. 2023. Non-muscle myosin 2 at a glance.
800 *J Cell Sci* 136:jcs260890. doi:10.1242/jcs.260890
801 30. Quintanilla MA, Patel H, Wu H, Sochacki KA, Chandrasekar S, Akamatsu M, Rotty
802 JD, Korobova F, Bear JE, Taraska JW, Oakes PW, Beach JR. 2024. Local
803 monomer levels and established filaments potentiate non-muscle myosin 2
804 assembly. *J Cell Biol* 223:e202305023. doi:10.1083/jcb.202305023
805 31. Rossman KL, Der CJ, Sondek J. 2005. GEF means go: turning on RHO GTPases
806 with guanine nucleotide-exchange factors. *Nat Rev Mol Cell Biol* 6:167–180.
807 32. Salbreux G, Charras G, Paluch E. 2012. Actin cortex mechanics and cellular
808 morphogenesis. *Trends Cell Biol* 22:536–545. doi:10.1016/j.tcb.2012.07.001
809 33. Small JV, Stradal T, Vignal E, Rottner K. 2002. The lamellipodium: where motility
810 begins. *Trends Cell Biol* 12:112–120. doi:10.1016/S0962-8924(01)02237-1
811 34. Spiering, D. *et al.* (2013) 'Quantitative ratiometric imaging of fret-biosensors in
812 living cells', *Methods in Cell Biology*, pp. 593–609. doi:10.1016/b978-0-12-
813 407761-4.00025-7.
814 35. Stringer C, Pachitariu M. 2024. Cellpose3: one-click image restoration for
815 improved cellular segmentation. doi:10.1101/2024.02.10.579780
816 36. Virtanen P, Gommers R, Oliphant TE, Haberland M, Reddy T, Cournapeau D,
817 Burovski E, Peterson P, Weckesser W, Bright J, van der Walt SJ, Brett M, Wilson
818 J, Millman KJ, Mayorov N, Nelson ARJ, Jones E, Kern R, Larson E, Carey CJ,
819 Polat İ, Feng Y, Moore EW, VanderPlas J, Laxalde D, Perktold J, Cimrman R,
820 Henriksen I, Quintero EA, Harris CR, Archibald AM, Ribeiro AH, Pedregosa F, van

Mulbregt P. 2020. SciPy 1.0: fundamental algorithms for scientific computing in Python. *Nat Methods* 17:261–272. doi:10.1038/s41592-019-0686-2

37. Wilson CA, Tsuchida MA, Allen GM, Barnhart EL, Applegate KT, Yam PT, Ji L, Keren K, Danuser G, Theriot JA. 2010. Myosin II contributes to cell-scale actin network treadmilling through network disassembly. *Nature* 465:373–377. doi:10.1038/nature08994

38. Wood KM, Smith CJ. 2021. Clathrin: the molecular shape shifter. *Biochem J* 478:3099–3123. doi:10.1042/BCJ20200740

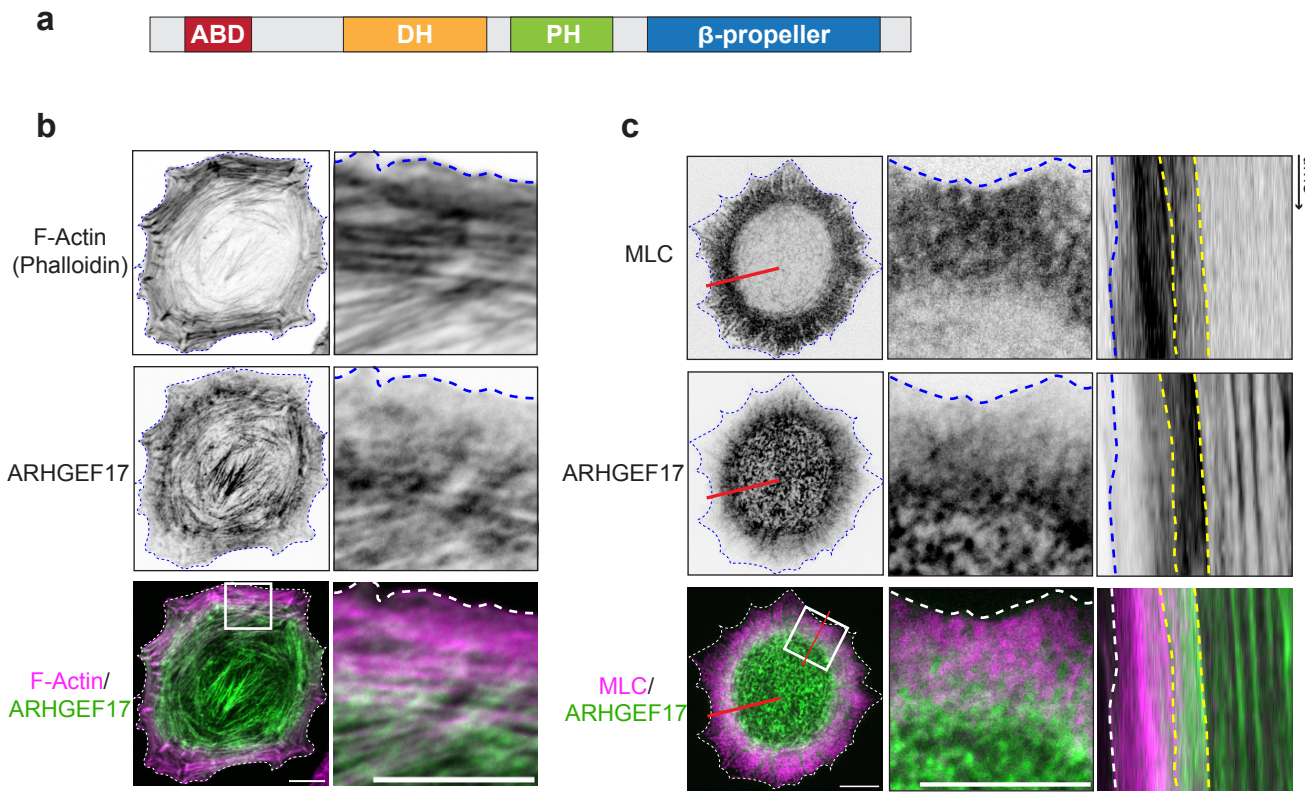

Figure 1. ARHGEF17 Structure, subcellular localization and dynamics
A: Scheme of the domain structure of ARHGEF17. (ABD : Actin Binding Domain)
B,C,D: Images are shown with inverted black and white contrast (ibw), or overlayed channel color-coded images are shown.
B: Confocal images of a spreading REF52 expressing ARHGEF17-mCherry and immunostained with Phalloidin. Left panels: whole cell. Right panels: magnified insets from boxes
C: Spinning disk confocal timelapse imaging of a spreading REF52 cell expressing ARHGEF17-GFP, and MLC-mCherry. Right panel: Kymograph analysis of both signals along the line drawn in red in the left panel.
Scale bars: 10 µm

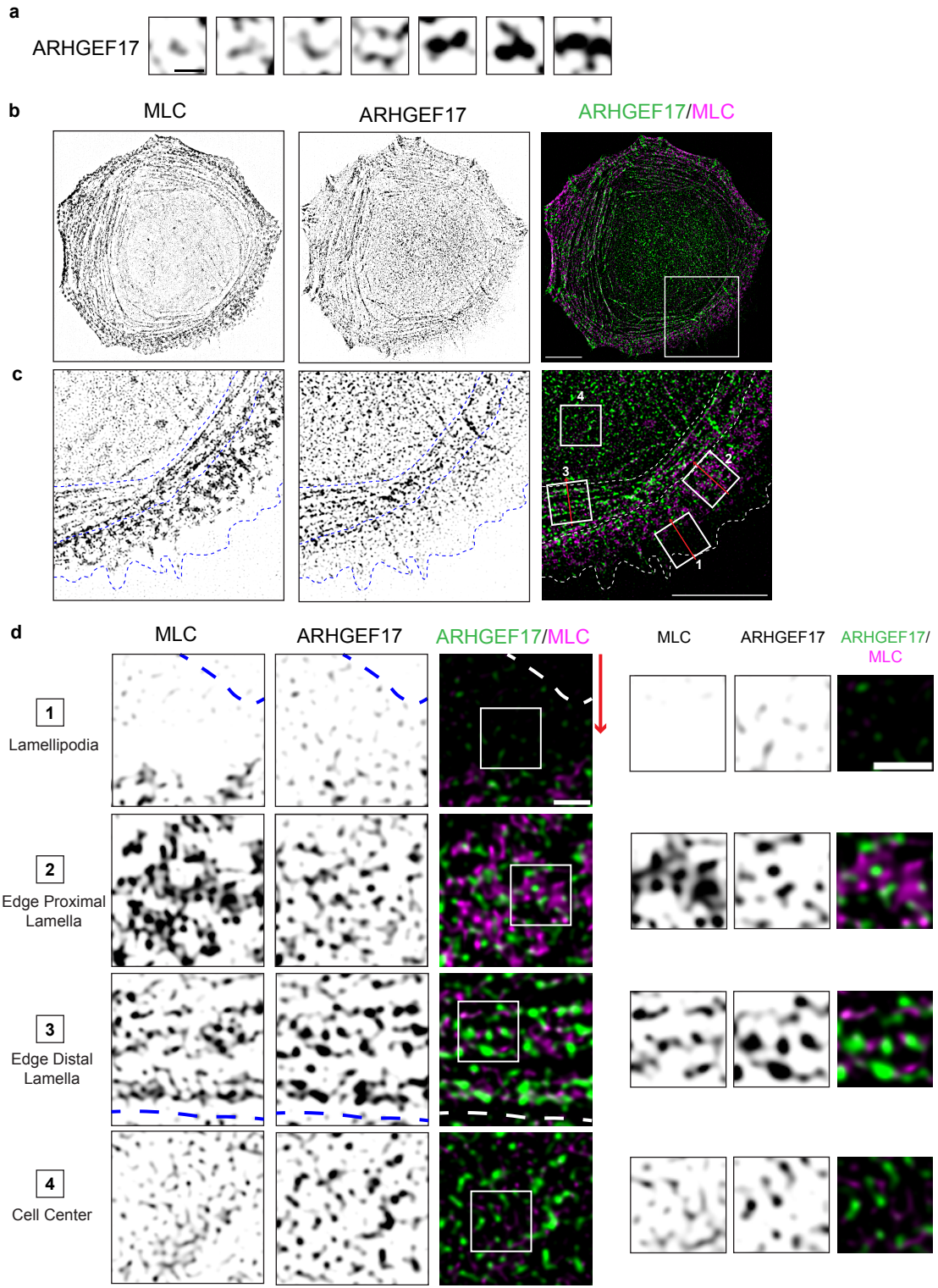

Figure 2: SIM imaging of ARHGEF17 and Myosin Light Chain subcellular localization.
All images come from SIM imaging of a spreading REF52 fibroblast expressing ARHGEF17-GFP and MLC-mCherry. Ibw of single channels or color-coded overlays are shown.
A: Gallery of ARHGEF17 clusters document their oligomerization properties.
B: ARHGEF17/MLC subcellular localization over the whole cell.

C: High magnification panel of A. Dotted lines delineate the cell edge, the interface between the contractile and low-contractile lamella regions, the low contractile lamella with the cell center.
D: High magnification panels from C. Note that the panels have been oriented to be parallel to the edge, with the retrograde actin flow being oriented from top to bottom (denoted by the red arrow). Additional magnified insets on the right panels provide intuition about the ultrastructure of the MLC and ARHGEF17 arrays. Inset 1: Lamellipodium, inset 2: edge proximal contractile lamella, inset 3: edge distal low contractile lamella, inset 4: cell center.
Scale bars: (A) 0.5 μm, (B,C) 10 μm, (D) 1 μm.

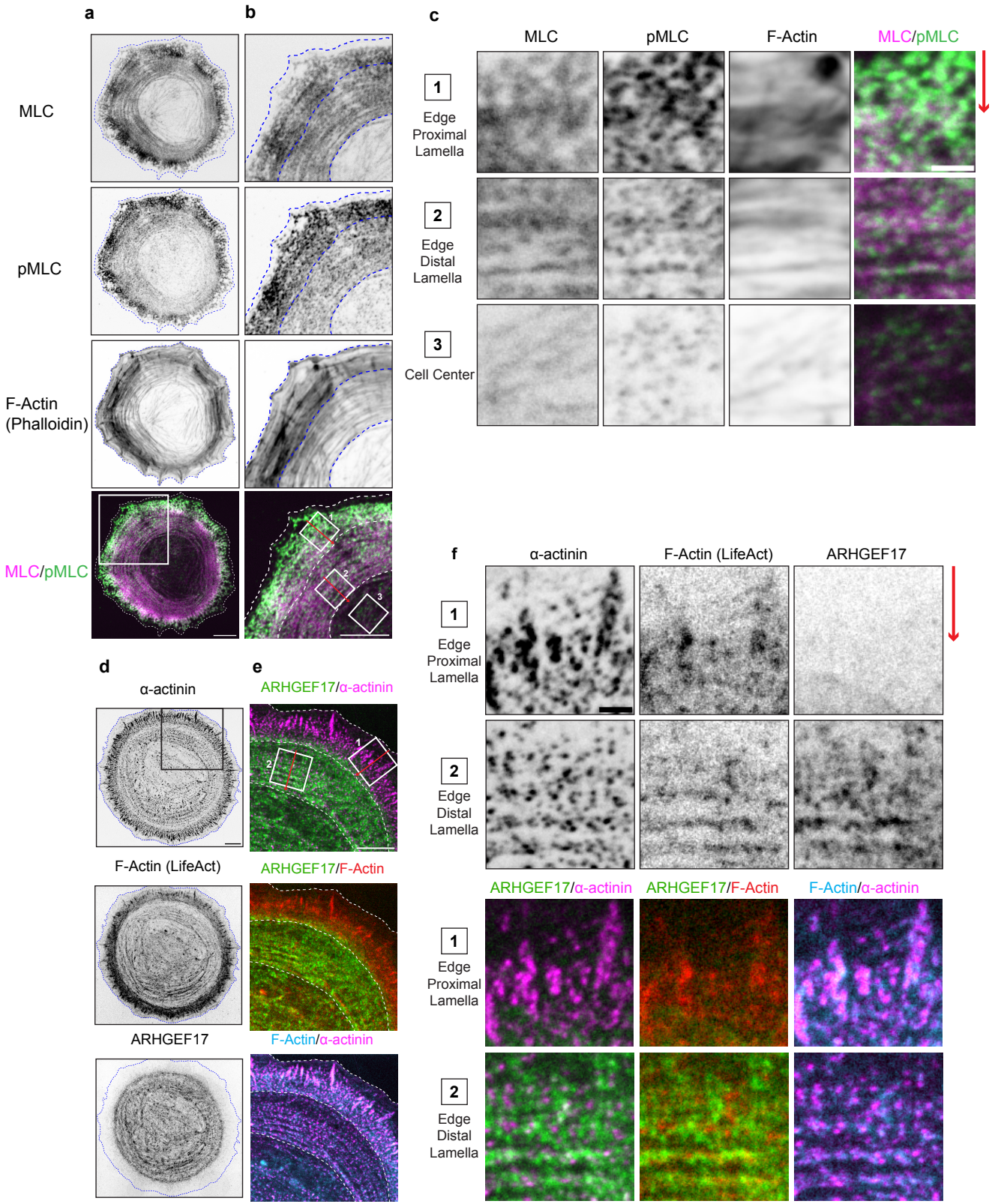

Figure 3: Subcellular localisation of MLC/MLC phosphorylation and ARHGEF17, F-actin and a α-actinin. A-C Confocal imaging of a spreading REF52 cell expressing MLC-mCherry and immunostained with pMLC and Phalloidin.

A: Global view of the cell
B: Magnification panel of the inset shown in (A)
C: High magnification panels of the insets shown in (B). Inset 1: edge proximal contractile lamella, inset 2: edge distal low contractile lamella, inset 3: cell center.
D-F: Confocal imaging of spreading REF52 cells expressing ARHGEF17-mCherry and LifeAct-miRFP and immunostained with α-actinin.
D: Global view of the cell
E: Magnification panel of the inset shown in (D)
F: High magnification panels of the insets shown in (E). Inset 1: edge proximal contractile lamella, inset 2: edge distal low contractile lamella
Ibw of single channels or color-coded overlays are shown. Note that the panels of (C) and (F) have been oriented to be parallel to the edge, with the retrograde actin flow being oriented from top to bottom (denoted by the red arrow).
Scale bars: (A-B) 10 µm, (C) 2 µm, (D) 10 µm, (F) 2 µm

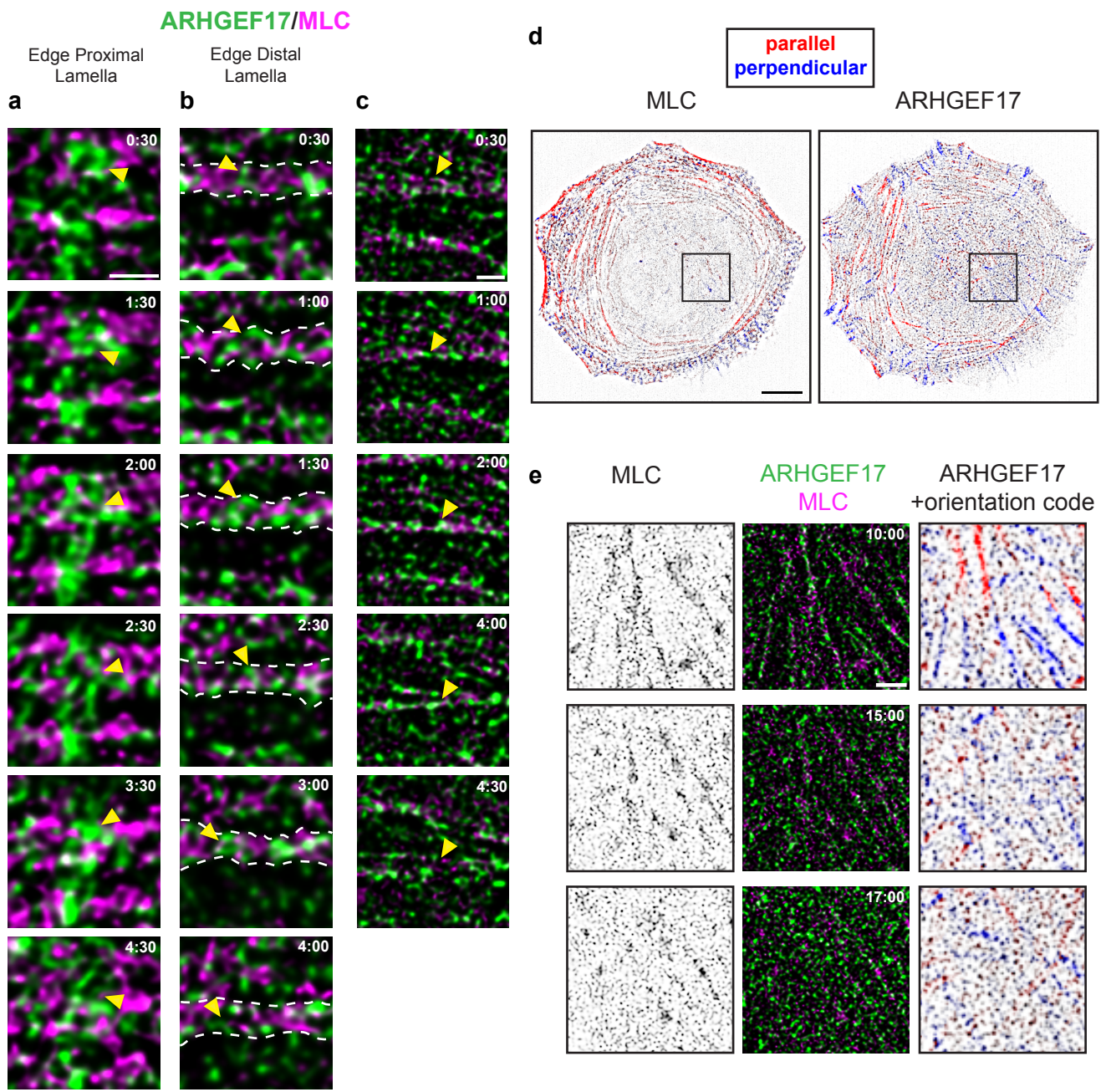

Figure 4: SIM imaging of ARHGEF17 and Myosin Light Chain dynamics.
SIM imaging
SIM timeseries of the same cell shown in Figure 2 are shown.
A,B: High resolution time series micrographs of ARHGEF17 and MLC dynamics in the edge proximal contractile (A) and edge distal low contractile lamella (B).
C: Timeseries micrographs of ARHGEF17 and MLC dynamics in the low contractile edge distal lamella with an example of transverse arc disassembly.
D: Analysis of correlated orientation of Myosin filaments (MLC) and ARHGEF17 clusters as analyzed using orientation-py. Correlated fluorescence signals that are parallel/perpendicular to the edge are color-coded in red and blue respectively. Ibw contrast is shown.
E: Timeseries micrographs of the disassembly of an actomyosin fiber in the cell center by ARHGEF17. Left panel: MLC (Ibw contrats), Middle panel: ARGEF17/MLC overlay, right panel: ARHGEF17 + orientation code.
Scale bars: (A-B-C) 1 µm, (D) 10 µm, (E) 2 µm

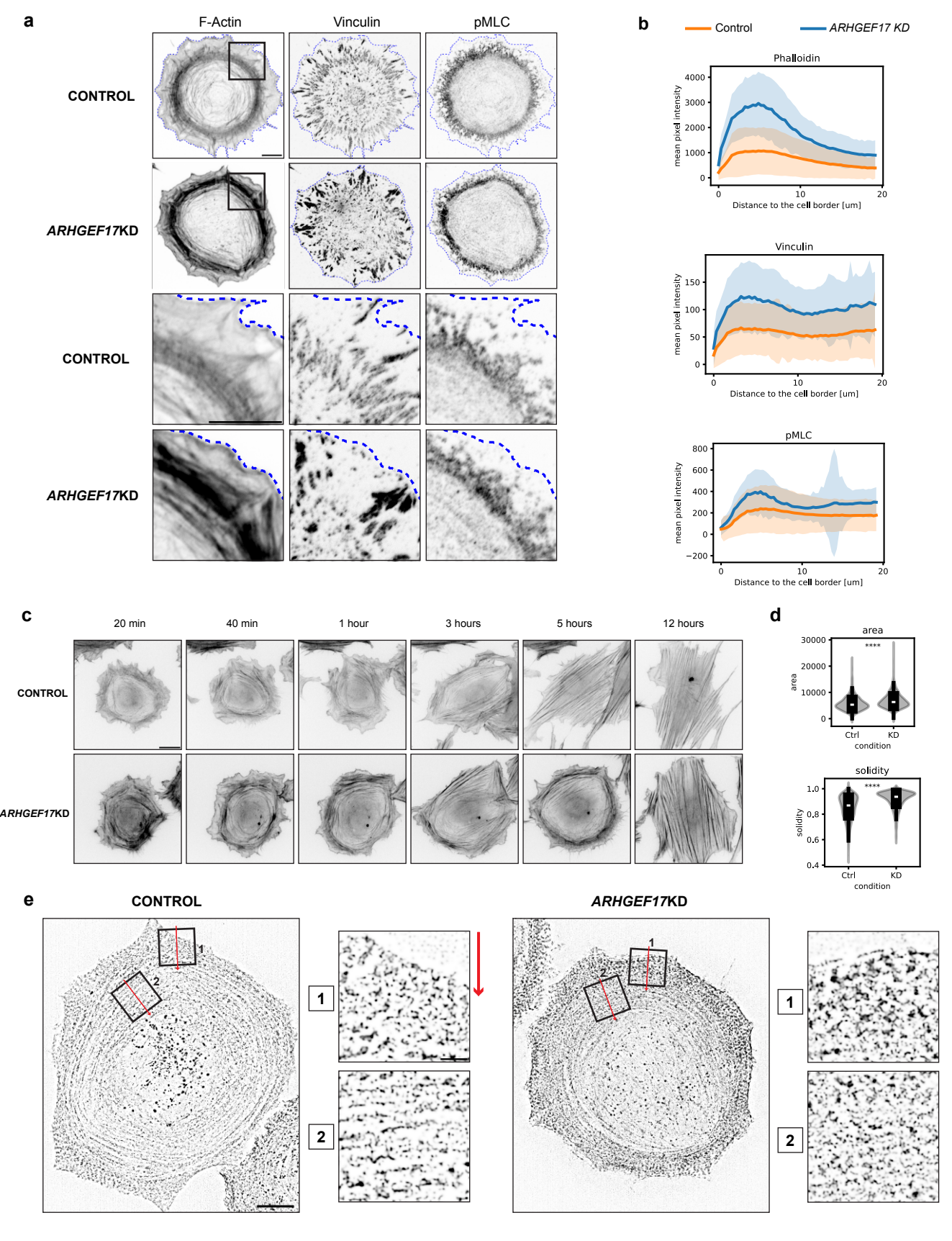
a
F-Actin
Vinculin
pMLC
CONTROL
ARHGEF17KD
CONTROL
ARHGEF17KD
b
Control
ARHGEF17 KD
Phalloidin
mean pixel intensity
Distance to the cell border [um]
Vinculin
mean pixel intensity
Distance to the cell border [um]
pMLC
mean pixel intensity
Distance to the cell border [um]
c
20 min
40 min
1 hour
3 hours
5 hours
12 hours
CONTROL
ARHGEF17KD
d
area
****
area
Ctrl
KD
condition
solidity
****
solidity
Ctrl
KD
condition
e
CONTROL
ARHGEF17KD
1
2
1
2
1
2
1
2

Figure 5: Effects of ARHGEF17 siRNA KD in REF52 cells

A: Fluorescence micrographs of cells stained with Phalloidin (F-actin), Vinculin and pMLC specific antibodies showing the impact of ARHGEF17 KD on cell morphology during spreading. Cells were detached, allowed to spread for 1 hour on fibronectin-coated coverslips. Images acquired using a 100x planApo oil immersion objective.

B: Quantification of phalloidin, pMLC and vinculin fluorescence intensities in control and ARHGEF17 KD cells (Images acquired using a 100x objective). Distance intensity plots are shown for intensity of staining from cell border towards cell center. Shaded area indicates standard deviation. n= 477 cells (242 Control, 235 KD).

C: Time-lapse series showing cell spreading and polarisation in control versus ARHGEF17 KD cells. Increased spreading and robust contractile F-actin structures are noted in KD cells within the first five hours as compared to control cells. At 12 hours, thicker contractile fibers are observed in ARHGEF17 KD cells.

D: Quantitative analysis of area and solidity of control and KD cells after 5 hours of spreading, measured at time point 5 hours. Boxplot with interquartile ranges and superimposed violin plots are shown to provide an intuition about the measurement distributions. White bar indicates population average. n=2033 (945 Control, 1088 KD). Statistical test: Mann-Whitney U test.

E: SIM images of spreading cells expressing MLC-mCherry in control and ARHGEF17 KD cells. High magnification panels showing (1) MLC in edge proximal lamella (2) MLC in edge distal lamella. The panels have been oriented to be parallel to the edge, with the retrograde actin flow being oriented from top to bottom (denoted by the red arrow).

Scale bars : (A) 10 µm, (C) 5 µm, (E) 10 µm, (E) Insets: 2 µm

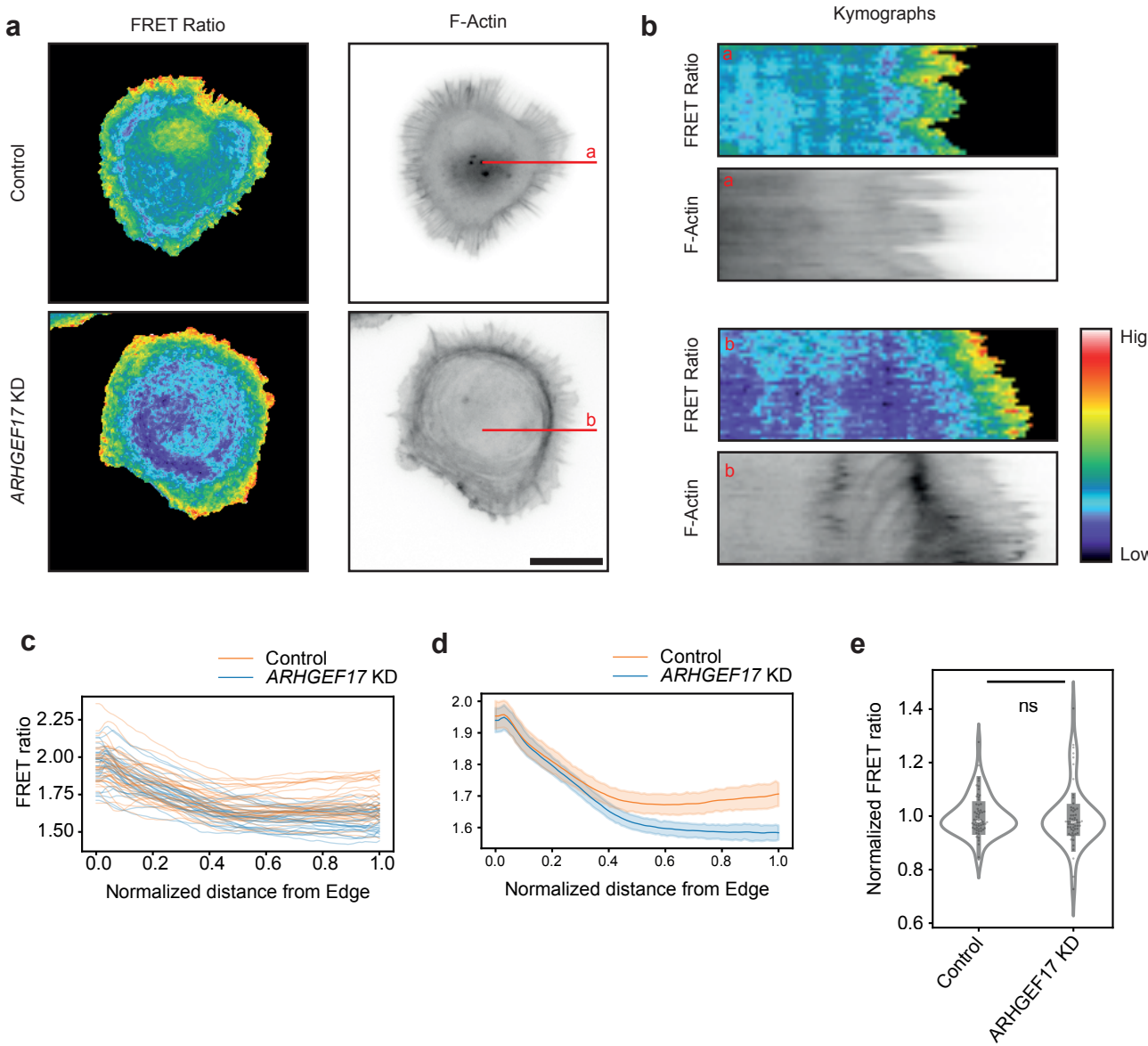

Figure 6: RhoA activity patterns in control versus ARHGEF17 KD cells.
A: Ratio images of RhoA2G FRET signals and Lifeact-mCherry F-actin in control versus ARHGEF17 KD cells. Ratio images are color-coded according to the color scale shown in (B). Lifeact-mcherry image is shown in inverted black and white contrast.
B: Kymograph analysis of the image in (A) along the red line.
C: Distance intensity RhoA FRET ratio plots are shown for single cell (see material and methods image analysis section). n=34 cells per condition.
D: Averaged distance RhoA FRET ratio plots. n=34 cells per condition. Shaded region indicates 95% confidence interval.
E: Measurements of RhoA FRET ratio cell averages. Measurements are normalized to the median value of the control. A t-test was used to assess statistical significance.
Scale Bar: (A) 50 µm.

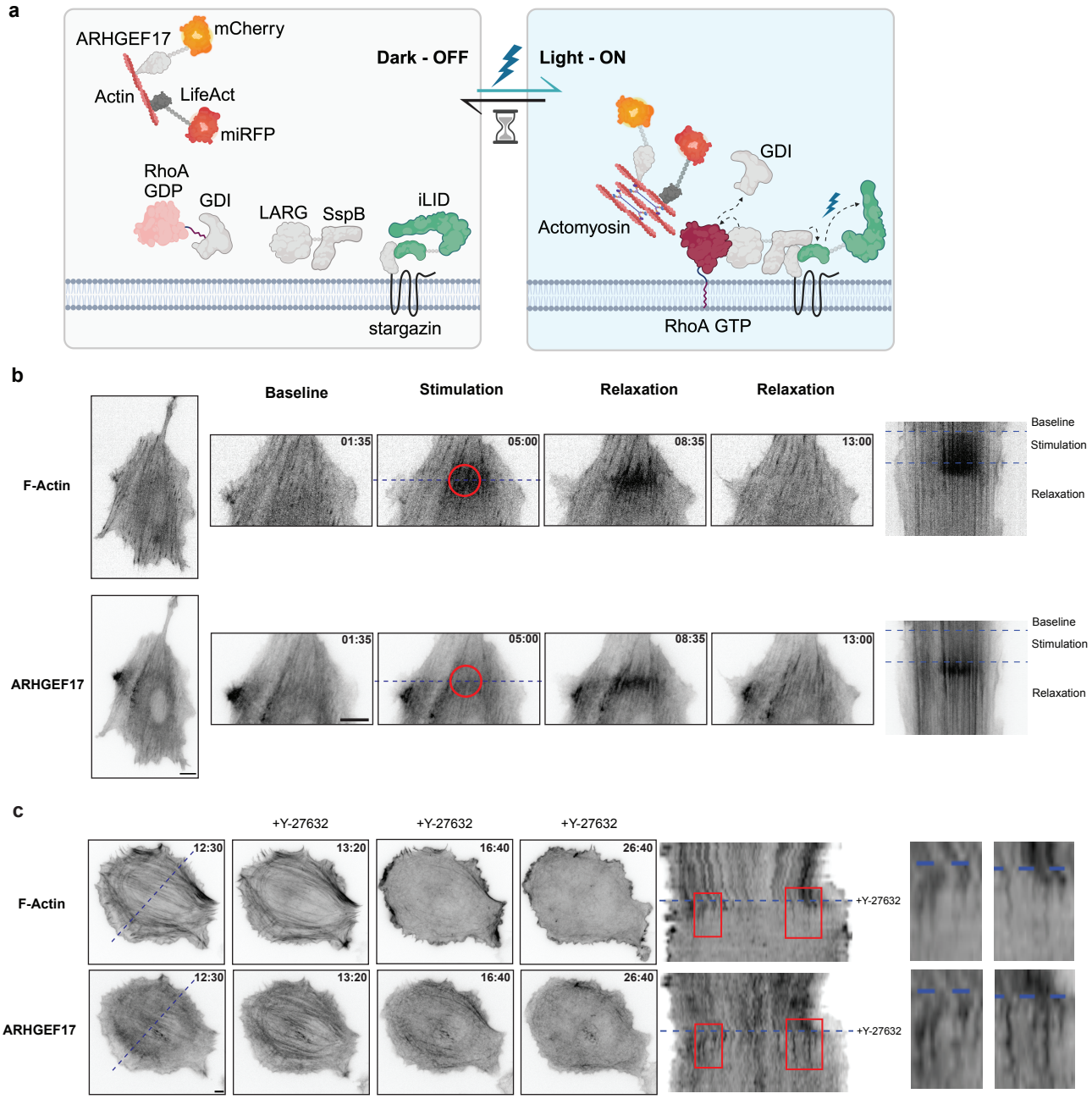

Figure 7: Mechanosensitivity of ARHGEF17 interaction with Actomyosin Network
A: Diagram of the optogenetic setup to study ARHGEF17 dynamics in response to a pulse of contractility. OptoLARG is an ILID-based optogenetic actuator to locally control Rho-mediated contractility and can be used with spectrally orthogonal mCherry tagged ARHGEF17 and the F-actin marker LifeAct-miRFP (adapted from Heydasch et al., 2023).
B: Cells activated locally by blue light to induce actomyosin contraction and relaxation, illustrating ARHGEF17 binding during actomyosin disassembly rather than assembly. Time in mm:ss.
C: Observations under ROCK kinase inhibitor Y-27632, showing ARHGEF17 transiently binds to disassembling actomyosin network. Time in mm:ss
Scale bars: (B-C) 10 µm

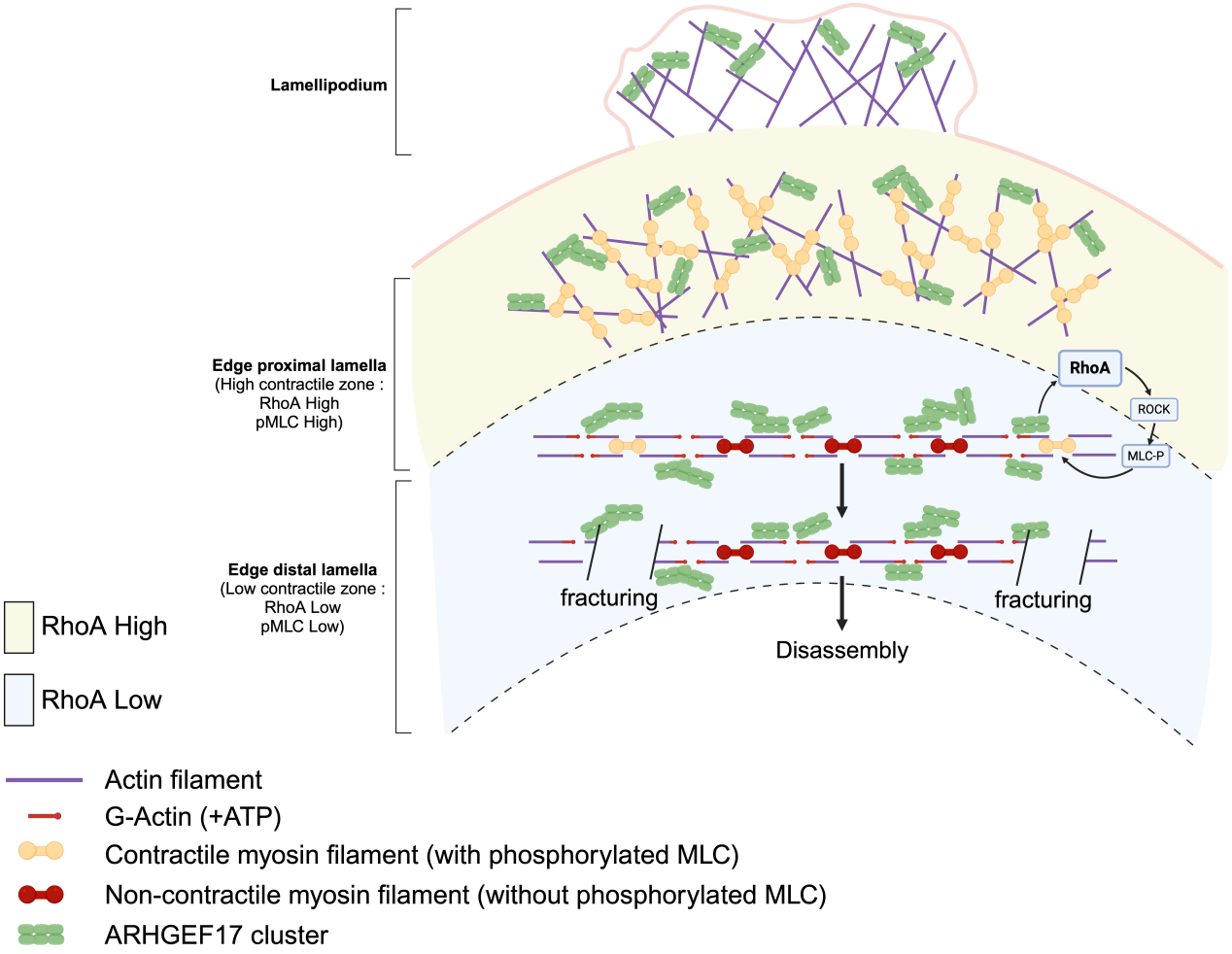

Figure 8: Model of ARHGEF17-mediated spatio-temporal regulation of lamella actomyosin network disassembly.
Note that all myosin filaments and ARHGEF17 clusters are shown so as not to overload the model.
1. ARHGEF17 clusters start to interact with F-actin filaments in the lamellipodium and are transported backwards with the actomyosin retrograde flow. ARHGEF17 clusters most likely interaction with ATP-actin at barbed ends.
2. In the edge proximal lamella, RhoA activity regulated by GEFs/GAPs that remain to be discovered induce MLC phosphorylation through activation of ROCK, resulting in strong actomyosin contractility. ARHGEF17 clusters continue to be transported backwards, and increase in density through an advection mechanism.
3. In the edge distal lamella, the actomyosin network relaxes because it transitions into the region of lower RhoA activity, leading to MLC dephosphorylation. Most myosin filaments most likely only act as crosslinkers, without exerting tension. ARHGEF17 localizes to barbed ends of F-actin filaments crosslinked by both non contractile myosin filaments and alpha-actinin. High ARHGEF17 concentration locally applied to the non contractile actomyosin network leads to its disassembly, most likely by fracturing the actomyosin lattice.